

Making Chemical Sense of Phase in Soft X-ray Spectroptychography

Joseph Stitsky¹, Jian Wang^{1,2}, Stephen Urquhart¹

1. Department of Chemistry, University of Saskatchewan, Treaty 6 Territory, Saskatoon, SK
2. Canadian Light Source, University of Saskatchewan, Saskatoon, SK

Highlights:

- Soft x-ray spectroptychography provides chemical information through absorption and phase.
- Phase spectra reveal chemical information in an indirect manner.
- The Kramers-Kronig relation is useful for understanding contrast in ptychography chemical analysis.

Abstract

Spectroptychography is being used to realize a significant improvement in the spatial resolution of x-ray spectromicroscopy, allowing chemical microanalysis at finer spatial scales. The chemical sensitivity of near edge X-ray absorption fine structure (NEXAFS) is familiar to most researchers who use x-ray spectromicroscopy for chemical microanalysis. However, the additional phase information available through ptychography provides additional and tantalizing data, and potentially additional chemical information. This paper explores the chemical information available in phase for a system of silicon dioxide nanospheres.

Keywords: spectroptychography, NEXAFS, x-ray microscopy, phase spectroscopy, chemical imaging

1. Introduction

Over the last quarter century, soft X-ray spectromicroscopy has grown in reach and application with the development of new instruments, improved focusing optics, *in situ* and *operando* sample environments, and statistical data analysis methods.[1-3] Most soft X-ray scanning transmission X-ray microscopy (STXM) microscopes owe their functionality to Fresnel zone plates, which provide a typical spatial resolution of 30 nm.[1] However, there is limited room for further reduction in the zone plate focused spot size and the spatial resolution of STXM microscopes, as the fabrication of zone plates that combine high efficiency with a high aspect ratio is a major nanofabrication challenge. An emerging X-ray microscopy variant, *ptychography*, has the potential to further increase the spatial resolution of X-ray microscopy. When used for X-ray spectroptychography, this computational imaging method provides an additional spectroscopic signal, phase.[3]

X-ray spectromicroscopy and x-ray spectroptychography methods combine chemical information from near-edge X-ray absorption fine structure (NEXAFS) spectroscopy with X-ray imaging. This combination is accomplished through imaging at specific X-ray energies (x, y ; fixed eV), NEXAFS spectroscopy of defined points (eV; x, y) or lines (eV, $x; y$), or through image sequences (x, y, eV)[4] that can be subsequently processed to extract spatially-resolved NEXAFS spectra and chemical maps. In the past 25 years, X-ray spectromicroscopy has developed from use in single-energy chemical contrast imaging[5] to the exploration of high-dimensional datasets (x, y, eV, ϕ , etc.) as image alignment methods,[4] stability through interferometry feedback methods,[6] and high coherent flux from synchrotron beamlines have improved the speed and fidelity of these measurements.

Spectromicroscopy image processing has also improved with the advancement of data analysis methods (clustering, principle component analysis, etc.).[7] X-ray spectromicroscopy is now routinely applied to samples in *in situ* and *operando* modes.[8-11] These advanced sample environment and processing methods translate directly to X-ray spectroptychography, with the added benefit of higher spatial resolution and an ability to exploit the additional 'phase' signal.

Ptychography[12-14] is a computational imaging technique based on the diffraction of coherent radiation by a non-crystalline sample. In this method, a series of far-field diffraction patterns are collected from overlapping

sample regions. These diffraction datasets are iteratively reconstructed using a phase-retrieval algorithm, which provides a complex (e.g. amplitude and phase) function for the sample and the probe.[12-15] Redundancy from the use of overlapping regions adds a numerical constraint that helps the reconstruction converge. Ptychography reconstruction algorithms are the subject of extensive review and discussion elsewhere,[12, 13] and will not be discussed in detail here. Ptychographic imaging is able to surpass the limits of optical aberration and numerical aperture imposed by traditional X-ray lenses as the spatial resolution is largely determined by the maximum angular range of the X-ray diffraction collection.[16] Significant improvements relative to zone-plate imaging have been reported; as an example see Shapiro *et al.*[17]

An outcome of ptychography reconstruction is simultaneous access to the phase and amplitude signal (in transmission) for the sample. Phase and absorption spectra are related to each other by the Kramers-Kronig relations,[18, 19] where the index of refraction, n , is given by

$$n = 1 - \delta - i\beta = 1 - \alpha\lambda^2(f_1 + if_2) \quad (1)$$

where δ is the refractive index decrement (related to dispersion or phase), β is the absorption index,[20] λ is the wavelength, and f_1 and f_2 are the atomic scattering factors for phase and absorption respectively. The constant α is given by:

$$\alpha \equiv \frac{r_e}{2\pi} n_a \quad (2)$$

where r_e is the classical electron radius and n_a is the number density of atoms.[19] The atomic scattering factor f_2 is related to the atomic absorption cross section (σ_a) by:

$$f_2 = \frac{\sigma_a}{2r_e\lambda} \quad (3)$$

The atomic scattering factors f_1 and f_2 are related to each other by the Kramers-Kronig relations, e.g.,

$$f_1(E) = Z + \frac{2}{E} \int_0^\infty \frac{\varepsilon^2 f_2(E)}{E^2 - \varepsilon^2} d\varepsilon \quad (4)$$

Here, the relativistic correction to Z , the atomic number, is neglected at soft X-ray wavelengths.[18, 20-22]

Phase is often exploited as a contrast mechanism in hard X-ray microscopy as absorption contrast is comparatively weak.[19] Absorption contrast is more frequently used at soft X-ray wavelengths, but phase has

tantalizing potential. Phase can be used to improve image contrast for samples that have weak absorption contrast. Absorption contrast (β) typically decreases with the fourth power of the photon energy while phase contrast (δ) scales with the inverse square of the energy.[23, 24] Jacobsen *et al.* have suggested that phase contrast imaging could provide chemical state imaging for a lower radiation dose, as a strong phase signal is seen at and below the rising edge of strong absorption peaks.[18] However, we are unaware of experiments exploiting this prediction, and note that the pre-edge 'phase' signal acquired at a few energies has limited chemical sensitivity relative to a full NEXAFS absorption or phase spectrum.

There are many examples of 'unusual phase contrast' in soft X-ray ptychography experiments, but not all researchers comment on the contrast present in their data. Maiden *et al.* compared absorption and phase contrast for Balb/3T3 mouse fibroblast cells that were doped with CoFe_2O_4 nanoparticles and suggested that the complementary information from phase can be more sensitive to chemical changes.[25] Shapiro *et al.* observed a halo around LiFePO_4 crystallites which they attributed to carbon photodeposition, and noted that this artefact was not visible in absorption images.[26] Farmand *et al.* combined absorption and phase contrast to provide near-edge X-ray refraction fine structure contrast, and exploited the energy dependent scattering cross-section to increase the spatial resolution of ptychography at resonant energies.[27]

Generally, phase images of samples obtained at near resonant energies tend to show an internal complexity not observed in absorption images. In this work, we focus on the sensitivity of X-ray spectroptychography to photodeposition and an unanticipated 'core-shell' effect in SiO_2 nanospheres. The photodeposition artefact appears at a wide range of X-ray energies and is a useful proxy for chemical contrast within spectroptychography. While the variation in phase signal with energy is tantalizing for the curious spectroscopist, absorption spectroscopy continues to provide a more direct approach for chemical microanalysis. Discrete electronic transitions in NEXAFS spectra are assigned in terms of specifically core \rightarrow valence or core \rightarrow multiplet transitions, with a direct chemical, structural or electronic interpretation and modelling through electronic structure calculations.

By virtue of the Kramers -Kronig relations, the chemical information of NEXAFS spectroscopy is embedded in the phase spectra. However, open questions remain about the accessibility and relative sensitivity of the chemical information within these phase spectra. One of the underlying goals of this study is to better understand how ptychography-derived phase spectra can be used for chemical microanalysis, complementary to absorption spectroscopy. In this paper, we examine the sensitivity of absorption and phase spectroscopy to photodeposition and chemical variation in ordered monolayer arrays of SiO₂ nanospheres. Photodeposition provides a useful 'unknown' for this exploration, and an energy-specific 'core-shell' effect was a fortuitous surprise that could only be observed with the improved spatial resolution of ptychography. These experimental spectra are interpreted with the aid of modelling with atomic cross-sections and the Kramers -Kronig relation.

2. Experimental

2.1 Samples

A solution of 220 nm SiO₂ nanospheres was obtained from Professor Tim Kelly of the University of Saskatchewan. Briefly, these nanospheres were prepared by combining 3.8 mL of NH₄OH, 7.2 mL of H₂O, 82.7 mL of C₂H₅OH and 6.3 mL of Si(C₂H₅O)₄ and stirring the mixture at 1000 rpm under Argon overnight. This solution was then centrifuged at 10,000 g and then titrated three times with 80 mL of deionized H₂O. The nanospheres were redispersed by sonication in 150 mL of deionized H₂O to yield the nanosphere solution. A dilution was prepared for deposition by combining 4 µL of this solution and 4.29 mL of Millipore water in a vial.

The SiO₂ nanosphere arrays were prepared by depositing a drop of this dilution onto a 100 nm thick Si₃N₄ membrane (Norcada Inc.). Solution evaporation was slowed by placing the sample membrane in an enclosed volume with an additional warm water source. After ~3 hours of slow evaporation, the remaining solvent was withdrawn from the membrane using the edge of a Kimwipe. The sample membrane then left to dry overnight within the enclosed environment.

The sample membranes were examined by Scanning Electron Microscopy (Hitachi SU8010 field emission SEM at the Western College of Veterinary Medicine) to ensure suitable coverage and to identify good sample areas for X-ray microscopy analysis.

2.2 Spectroptychography Measurements

Spectroptychography measurements were carried out using the ambient STXM at the 10ID-1 SM beamline of the Canadian Light Source (CLS).[28] For these measurements, the zone plate to sample distance was modified to create a larger diameter defocused beam spot on the sample, typically around 2 μm . The sample was raster scanned through this beam spot with a spacing that ensured sufficient overlap of scanned areas. Diffraction data was recorded for each point in the raster scan using either a Tucsen Dhyana 95V2 BSI sCMOS camera or an Andor DX434 CCD camera. X-ray spectroptychography data was obtained by performing ptychography scans at a series of X-ray energies. Full scan details are provided in the supplementary information. The monochromator energy scale for the O 1s scan was calibrated by aligning the characteristic pre-edge peak in the I_0 spectrum of the beamline (measured as 530.7 eV) to a known energy (531.7 eV).

2.3. Ptychography Reconstruction

All ptychography reconstructions were performed using the program PyPIE,[29] which employs the ePIE algorithm.[30-32] Reconstructions were performed with the master-slave ePIE reconstruction method, which uses two modes to represent a beam spot that is not fully coherent.[33] Amplitude (transmission) and phase images obtained from each reconstruction were processed into image sequences and aligned with the aXis2000 program,[34] which was used to extract spatially-resolved amplitude and phase spectra. Amplitude spectra were converted to optical density spectra using Beer's law, $OD = -\ln(I/I_0)$, if a reliable I_0 signal could be obtained from an uncontaminated and open sample area on the silicon nitride membrane.

2.4. Kramers – Kronig Relation Calculations

Several researchers have developed computer programs that convert NEXAFS spectra to phase spectra via the Kramers-Kronig relation.[18, 22] To explore trends in the atomic absorption and phase spectra of specific compounds, we have developed a simple code based on the `scipy.fftpack.hilbert` library,[35] which allows us to create and transform arbitrary functions, including the atomic contribution to the NEXAFS absorption spectra of compounds. This code calculates the integral shown in equation 4 but neglects the Z-term and the constants. Therefore, the results of this calculation are not quantitative for phase, but will qualitatively reflect changes in phase associated with small chemical changes. Transmission (to match experimental amplitudes) and optical density (as an input to the Kramers-Kronig relation calculation) atomic cross-section spectra of specified model materials were determined from Henke atomic cross-section data[21] within the program `aXis2000`[34] over the energy range 10 eV – 3 keV. Material thickness and densities of these models are listed in Table 1. The complete process is described in the accompanying information.

The qualitative approach described above is restricted to the atomic cross-section for specified compounds. To examine hypotheses related molecular or bonding effects in the O 1s NEXAFS spectromicroscopy study of the SiO₂ nanospheres, we have used the `kk_gui` code of Jacobsen et al.[18] This code splices an experimental NEXAFS spectrum from a specific core edge – where the near edge features are related to chemistry and bonding – and matches this NEXAFS spectrum to the Henke atomic cross-section for the elemental composition of the compound. This combination provides the molecular features near the core edge and the atomic cross-section away from the core edge, allowing for the Kramers-Kronig relation calculation to apply over a wide energy range, thus minimizing artefacts from a narrow integration interval. In this work, O 1s NEXAFS spectra of SiO₂ nanospheres (extracted from the data described in §2.2 and 2.3) is superimposed on the atomic cross-sections of Si₅O₁₀ and Si₅O₈, which are intended to model the stoichiometry of SiO₂ and SiO_{1.6}, as justified in §3.

3. Results and Discussion

Figure 1 presents amplitude (transmission) and phase ptychography images for a close-packed array of 220 nm diameter SiO₂ nanospheres deposited on a Si₃N₄ membrane, recorded at a photon energy of 571 eV. This is one

of a set of images from a spectroptychography dataset recorded away from a core edge, so we could examine image contrast related to atomic absorption without the complexity of near-edge features. This was the third dataset recorded from this sample area; the red box shows the region of a previous scan in this area that induced significant photodeposition on the sample. Such photodeposition is commonly observed in X-ray microscopy, where photochemistry from the incident X-ray beam causes chemical contaminants that are physically adsorbed on the sample surface to become chemisorbed.[36] Photodeposition appears as a slight decrease in signal in the amplitude image and a noticeable increase in brightness in the phase image. The unstructured dark regions in the upper left of the amplitude image are attributed to the presence of a second layer of SiO_2 nanospheres and chemical artefacts. We will initially focus on well-ordered regions away from these artefacts, with and without photodeposition.

Figure 2 presents the measured amplitude (Figure 2a) and phase (Figure 2b) spectra extracted from the bare Si_3N_4 membrane and the Si_3N_4 membrane with a layer of photodeposition. Specific regions are documented in Figure S1 in the supplemental information. The slight dip at 577-579 eV is attributed to chromium absorption from the beamline optics. As expected, the amplitude of the Si_3N_4 membrane region with photodepositon is slightly lower than the amplitude of the Si_3N_4 membrane region without photodeposition, with a change from 0.96 to 0.86 at 572 eV for example attributed to the additional absorption by the photodeposited film.

The differences in phase are much larger; the Si_3N_4 membrane region with photodeposition has a positive phase shift of ~ 0.1 radians, while the bare membrane has a negative phase shift of ~ -0.2 radians. While the negative sign is not understood, the relative magnitude of the phase signal is. This trend is consistent with Figure 1 where the phase image shows a 'bright' photodeposit region and a 'dark' bare Si_3N_4 membrane region while the amplitude image shows a similar intensity for both regions.

Figure 3 presents the measured amplitude (Figure 3a) and phase (Figure 3b) spectra for a sample region with the SiO_2 nanospheres and the SiO_2 nanospheres with photodeposition. Specific regions are documented in Figure S2 in the supplemental information. At 572 eV, the amplitude decreases from 0.81 to 0.65 for the SiO_2 nanospheres

region with photodeposition, and the phase increases from +0.11 radians to +0.62 radians. As for the bare Si_3N_4 membrane, photodeposition results in a dramatic increase in observed phase.

Figure 4 contains the optical density spectra of the SiO_2 nanospheres, the SiO_2 nanospheres with contamination from photodeposition, and the photodeposition signal itself. These optical density spectra were obtained using an I_0 signal recorded through an area of the Si_3N_4 membrane that lacks photodeposition; such internally normalized spectra therefore lack a contribution from the Si_3N_4 membrane. The optical density of the photodeposit at 572 eV is ~ 0.11 OD, while the optical density of the photodeposit on the SiO_2 nanospheres is twice that, at ~ 0.22 .

The increased optical density of photodeposit on the SiO_2 nanospheres compared to the Si_3N_4 membrane is attributed to an increase in the number of available surfaces for photodeposition to occur upon. We hypothesize that photodeposition occurs via a two-step process: in step one, carbon-containing molecules are physisorbed onto the sample surface. In the second step, the absorption of a photon by the carbon-containing molecules leads to photofragmentation, and the resulting radical species then quickly react with and bond to the surface. As the experiment works in transmission, there are at least two surfaces onto which photodeposition might occur – the front and the back surface of the Si_3N_4 membrane. In the transmission column through the deposited SiO_2 nanospheres, there are two additional surfaces from the top and bottom of the nanosphere, except for the small region where the nanosphere contacts the membrane. The doubling of surfaces on which photodeposition can occur provides an explanation of the doubled photodeposition cross-section. This could provide an unusual contrast mechanism for samples with a complex or porous morphology.

Atomic cross-section calculations of transmission and phase are used to interpret the experimental data. Figure 5a presents the atomic transmission cross-sections of the 100 nm thick Si_3N_4 membrane, with and without a 1 nm carbon film intended to simulate photodeposition. Figure 5c presents the same data across a smaller energy range corresponding to the data in Figures 2-4. We note that y-axis intensities vary between the calculated transmission cross-sections and the experimental transmission amplitude, as transmission can be calculated as a fraction (0 to 1), while the experimental transmission amplitude is not normalized for the incident flux. As

expected, the transmission of the membrane with carbon photodeposition is slightly lower (0.2 %) at 572 eV.

Figures 5b and 5d present the qualitative phase spectra, obtained with the Kramers – Kronig relation described in §2.4, and are presented in arbitrary angular units. The phase difference is nearly imperceptible in the wide energy spectrum, but the phase of the sample with photodeposition is slightly higher (0.7%) at 572 eV.

Figure 6a and 6c present the atomic transmission cross-sections for a sample consisting of a 100 nm thick Si_3N_4 membrane and 220 nm thick SiO_2 layer, with and without a 3 nm carbon film intended to simulate photodeposition; Figure 6c presents a portion of the data shown in Figure 6a across a smaller energy range. Likewise, Figures 6b and 6d present the calculated qualitative phase spectra. Like the bare membrane, the transmission spectra vary by 0.6% with photodeposition, and the calculated phase spectra differ by 1% with photodeposition.

For both the bare membrane and the membrane region with samples, the phase spectra show a more positive phase and show a higher percent change in signal with photodeposition than the transmission spectra. These calculations are consistent with experiment, which shows a similar trend in transmission and phase signal.

In this example, the enhanced phase contrast from photodeposition that occurs away from core edges is chemically and spectroscopically relevant. This result indicates that artefacts will be revealed in non-obvious ways and shows the value of modelling phase through the Kramers-Kronig relations.

We now turn our attention to natural chemical variations of the material – an unexpected variation that provides an ‘unknown’ for this discussion. Figures 7 and 8 present data from a spectroptychography study of the SiO_2 nanospheres at the O 1s core edge. Figure 7 presents selected amplitude (a, b) and phase (c, d) images collected at 538.33 eV and 536.52 eV respectively. The left amplitude image (Figure 7a) was recorded at an energy corresponding to the maximum of the broad O 1s resonance for the SiO_2 nanospheres, as shown in Figure 8b. The nanospheres are clearly visible in this image, with darker spots corresponding to transmission through the thicker center of the spheres. Interestingly, an image recorded on the rising edge of the broad O 1s resonance – at 536.52 eV – shows a ‘shell’ visible on the edge of these SiO_2 spheres. This shell appears as a honeycomb shape in

the array of packed SiO₂ nanospheres. A larger diameter 'donut' in the upper right-hand corner of the images is presumed to be a photodeposition artefact from an unfocused beam spot illuminating the sample.

Careful extraction of the core and shell spectroscopic signals was performed; the resulting data is presented in Figure 8a for amplitude, in Figure 8b for optical density and in Figure 8c for phase. Specific regions are documented in Figure S3 in the supplemental information. While the optical density from the shell is lower than the core on account of the thinner edge of the nanospheres, a slight spectroscopic inversion is observed at 536.5 eV, corresponding to the images where the 'shell' is darkest. This weak pre-edge signal is attributed to an O 1s → $\sigma^*(\text{O-H})$ functionalization, as unreacted ethyl functionalization (e.g., Si-O-C₂H₅) on the surface of the SiO₂ nanospheres is expected to hydrolyse to form Si-O-H bonds. Transitions with O 1s → $\sigma^*(\text{Si-O-H})$ character are expected to appear at lower energy than transitions with O 1s → $\sigma^*(\text{Si-O-Si})$ character that are characteristic of the bulk of the SiO₂ nanospheres.

This shell structure has a clear chemical origin, as this feature appears at a specific X-ray energy and corresponds to a distinct resonant X-ray absorption process. This is an example of how spectroptychography – using the insights of spectroscopy to interpret ptychography – can be used to differentiate chemical origins of image contrast from physical effects, such as X-ray scattering from the edge of the nanospheres, or a potential breakdown of the thin object approximation in the ptychographic reconstruction. These effects may still be present in this dataset, but the extracted NEXAFS spectra show that the shell structure has a chemical origin.

It is difficult to draw chemical conclusions from the phase spectra presented in Figure 8c. The magnitude of the phase change for the shell is less than that of the core, and the phase spectra differ in their pre-edge background and shape. We see from the off-edge study of SiO₂ nanospheres (Figures 1-6), that variation in the concentration of other elements plays a significant role in the background intensity of the phase spectra.

The Kramers-Kronig relation allows us to perform spectroscopic "experiments" to try to understand the chemical origin of the phase spectra. A comparison of the O 1s optical density spectrum of the shell to that of the SiO₂ nanosphere bulk (Figure 8b) shows an approximate reduction in oxygen concentration of ~20%. As an experiment, we have examined the Kramers-Kronig relation for a sample of SiO₂ and a sample of SiO_{1.6} (e.g., a

20% reduction in oxygen), using Jacobsen's `KK_gui` code.[18] This code allows one to “paste” a near-edge spectrum (in this case, the O 1s spectrum of the SiO₂ nanospheres) into the atomic (Henke) photoabsorption cross-section for a defined composition, and then to transform it to obtain the corresponding f_1 atomic scattering factors for phase. This allows us to model changes in chemical composition to see if it explains the differences in the observed phase spectra.

Figure 9a presents the models for the O 1s NEXAFS spectrum of SiO₂ and SiO_{1.6}, where a representative oxygen 1s spectrum of SiO₂ nanospheres is superimposed into the atomic cross-section of an SiO₂ and SiO_{1.6} compound, using Jacobsen's `KK_gui` code.[18] The f_1 ‘phase’ atomic scattering factors obtained from the Kramers-Kronig relation are shown in Figure 9b. The phase data of the SiO_{1.6} model show a reduction in the relative intensity of the maximum and minimum of the phase relative to the SiO₂ model. However, the simulation does not match the magnitude of the change observed experimentally, in Figure 8c.

There are several possible reasons for the mismatch between experiment and simulation. As the chemistry of the core and shell are so similar, it is unlikely that the small difference in the absorption spectrum due to Si-O-H bonding would encode such a large difference in phase. The fidelity of the experimental data and the alignment of images in a sequence may degrade the extracted phase spectra. It seems most likely that there are chemical changes not accounted for in the simple model, such as a difference in elemental composition other than oxygen. The work on non-resonant ptychography of the photodeposition artefact shows that elemental composition differences impact the magnitude of the phase at energies far above the core edges of those elements. Therefore, it is possible that the phase spectrum of the shell is determined by unknown composition differences. Despite being partially inconclusive, this analysis shows that consideration of the full chemical composition of an analyte is needed to understand and quantify phase spectra, particularly when performing chemical characterization of unknown phases.

4. Conclusion

Absorption and phase spectra of an ordered array of SiO₂ nanospheres has been acquired using soft X-ray spectroptychography. The origin of an enhanced sensitivity of phase to photodeposition is characterized; the relative phase signal increase due to photodeposition is greater than the decrease in transmission signal. These results show how phase encodes small variations in chemical composition differently than transmission or optical density spectra.

The other observation about photodeposition – that it appears to be proportional to the number of surfaces in the transmission column – will be relevant in the examination of highly porous materials that are more prone to this artefact.

Phase encodes unique information for the study of ‘unknowns’, but a good hypothesis and modeling is required to access this information.

Declaration of Competing Interest

The authors do not have any competing interests.

Acknowledgement

Silicon oxide nanospheres were provided by Professor Tim Kelly of the University of Saskatchewan. Part of the research described in this paper was performed using Spectromicroscopy beamline at the Canadian Light Source (CLS). The CLS is supported by the Canada Foundation for Innovation (CFI), the Natural Sciences and Engineering Research Council (NSERC), the National Research Council (NRC), the Canadian Institutes of Health Research (CIHR), the Government of Saskatchewan, and the University of Saskatchewan. Recent upgrades to the Spectromicroscopy beamline were supported by CFI, the Provinces of Saskatchewan, Ontario and Alberta, and the Automobile Fuel Cell Cooperation (AFCC). Data analysis was performed using the HPC facilities of the University of Saskatchewan, the Canadian Light Source, and the Digital Research Alliance of Canada. SEM experiments were performed at the Western College of Veterinary Medicine Imaging Centre, with assistance from Dr. Li Yang. SGU is supported by NSERC. JS is supported by an NSERC-INSPIRE fellowship.

Data Availability

Urquhart, S., Joseph, S., Jian, W. (2023). Making Chemical Sense of Phase in Soft X-ray Spectroptychography. Federated Research Data Repository. <https://doi-org.cyber.usask.ca/10.20383/103.0778>.

Figure Captions

Figure 1: X-ray ptychography amplitude (a) and phase (b) images of a single-layer packed array of 220 nm SiO₂ nanospheres on a Si₃N₄ membrane recorded at a photon energy of 571 eV with a photodeposition artefact in the upper left-hand corner indicated by the red box. The scale bar in each image represents 1 μm.

Figure 2: Amplitude (a) and phase (b) spectra from sample free regions of the Si₃N₄ membrane, recorded from areas with photodeposition (Si₃N₄ + photodeposition) and without (Si₃N₄). The specific area from which these spectra are extracted is presented in the supplemental information.

Figure 3: Amplitude (a) and phase (b) spectra from the SiO₂ nanosphere array on the Si₃N₄ membrane, recorded from areas with photodeposition (Si₃N₄ + SiO₂ + photodeposition) and without (Si₃N₄ + SiO₂). The specific area from which these spectra are extracted is presented in the supplemental information.

Figure 4: Optical density NEXAFS spectra of the photodeposit on the blank Si₃N₄ membrane (photodeposition) and the SiO₂ nanosphere array on the Si₃N₄ membrane with (SiO₂ with photodeposition) and without (SiO₂) the photodeposit. These optical density spectra are obtained using Beer's law, where the I₀ spectrum is obtained from the Si₃N₄ membrane region without photodeposition. Because of the internal I₀ normalization, the optical density of the Si₃N₄ membrane does not appear.

Figure 5: Simulated atomic photoionization cross-section (a) for a model consisting of a 100 nm Si₃N₄ membrane with simulated photodeposition (Si₃N₄ + C) and without simulated photodeposition (Si₃N₄) based on Henke atomic cross-section data.[21] Phase spectra (b) calculated with the Kramers-Kronig relation with arbitrary angular units. Figures (c) and (d) are the same spectra for the region from 570 – 590 eV.

Figure 6: Simulated atomic photoionization cross-section (a) for a model consisting of a 220 nm thick SiO₂ layer on a 100 nm thick Si₃N₄ membrane, with simulated photodeposition (Si₃N₄ + SiO₂ + C) and without simulated photodeposition (Si₃N₄ + SiO₂), based on Henke atomic cross-section data.[21] The maximum thickness of the SiO₂ nanospheres is used for this analysis. Phase spectra (b) calculated with the Kramers-Kronig relation with arbitrary angular units. Figures (c) and (d) are the same spectra for the region from 570 – 590 eV.

Figure 7: X-ray ptychography amplitude (a,b) and phase (c,d) images of a single-layer packed array of 220 nm SiO₂ nanospheres on a Si₃N₄ membrane. Images (a) and (c) were recorded at 538.33 eV and images (b) and (d) were recorded at 536.52 eV. The scale bar in each image represents 0.6 μm.

Figure 8: Amplitude (a), Optical Density (b) and Phase (c) spectra from the core (SiO₂ NS Core) and shell (SiO₂ NS Shell) layers of the SiO₂ nanospheres. The specific area from which these spectra are extracted is presented in the supplemental information.

Figure 9: (a) Model O 1s NEXAFS spectra of SiO₂ and SiO_{1.6} generated by 'splicing' experimental NEXAFS data for the core and shell of the SiO₂ nanospheres, respectively into the atomic photoabsorption cross-section data for the corresponding chemical composition. (b) Model f_1 'phase' atomic scattering factors for the nanosphere core and shell obtained through the model O 1s NEXAFS data and the Kramers-Kronig relation.

Table 1: Input Parameters for Kramers – Kronig Relation Calculations

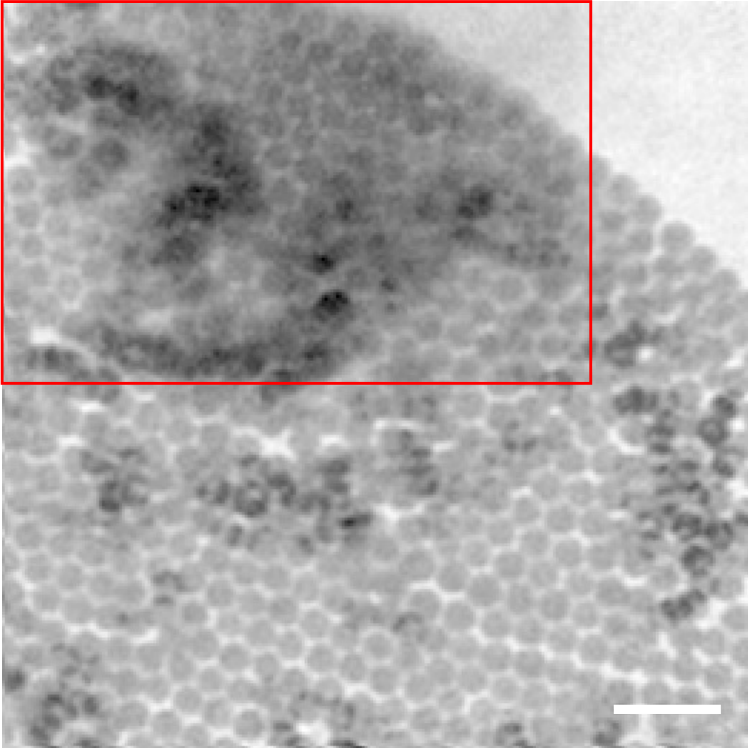
| Film | Component | Thickness | Density |
|---|--------------------------------|-----------|------------------------|
| Si ₃ N ₄ | Si ₃ N ₄ | 100 nm | 3.17 g/cm ³ |
| Si ₃ N ₄ + photodeposition | Si ₃ N ₄ | 100 nm | 3.17 g/cm ³ |
| | C | 1 nm | 2.15 g/cm ³ |
| Si ₃ N ₄ + SiO ₂ | Si ₃ N ₄ | 100 nm | 3.17 g/cm ³ |
| | SiO ₂ | 220 nm | 2.20 g/cm ³ |
| Si ₃ N ₄ + SiO ₂ + photodeposition | Si ₃ N ₄ | 100 nm | 3.17 g/cm ³ |
| | SiO ₂ | 220 nm | 2.20 g/cm ³ |
| | C | 3 nm | 2.15 g/cm ³ |

References

- [1] H. Ade, A.P. Hitchcock, NEXAFS microscopy and resonant scattering: Composition and orientation probed in real and reciprocal space, *Polymer* 49 (2008) 643-675.
- [2] A.P. Hitchcock, Soft X-ray spectromicroscopy and ptychography, *Journal of Electron Spectroscopy and Related Phenomena* 200 (2015) 49-63.
- [3] S.G. Urquhart, X-ray Spectroptychography, *ACS Omega* 7 (2022) 11521-11529.
- [4] Jacobsen, Wirick, Flynn, Zimba, Soft X-ray spectroscopy from image sequences with sub 100 nm spatial resolution, *Journal of Microscopy* 197 (2000) 173-184.
- [5] H. Ade, X. Zhang, S. Cameron, C. Costello, J. Kirz, S. Williams, Chemical Contrast in X-Ray Microscopy and Spatially Resolved XANES Spectroscopy of Organic Specimens, *Science* 258 (1992) 972-975.
- [6] A.L.D. Kilcoyne, T. Tyliszczak, W.F. Steele, S. Fakra, P. Hitchcock, K. Franck, E. Anderson, B. Harteneck, E.G. Rightor, G.E. Mitchell, A.P. Hitchcock, L. Yang, T. Warwick, H. Ade, Interferometer-controlled scanning transmission X-ray microscopes at the Advanced Light Source, *Journal of Synchrotron Radiation* 10 (2003) 125-136.
- [7] M. Lerotic, C. Jacobsen, T. Schäfer, S. Vogt, Cluster analysis of soft X-ray spectromicroscopy data, *Ultramicroscopy* 100 (2004) 35-57.
- [8] V. Prabu, M. Obst, H. Hosseinkhannazer, M. Reynolds, S. Rosendahl, J. Wang, A.P. Hitchcock, Instrumentation for in situ flow electrochemical Scanning Transmission X-ray Microscopy (STXM), *Review of Scientific Instruments* 89 (2018) 063702.
- [9] A.P. Hitchcock, C. Zhang, H. Eraky, L. Shahcheraghi, F. Ismail, D. Higgins, In-situ and Operando Studies with Soft X-Ray Transmission Spectromicroscopy, *Microscopy and Microanalysis* 27 (2021) 59-60.
- [10] J.T. Mefford, A.R. Akbashev, M. Kang, C.L. Bentley, W.E. Gent, H.D. Deng, D.H. Alsem, Y.-S. Yu, N.J. Salmon, D.A. Shapiro, P.R. Unwin, W.C. Chueh, Correlative operando microscopy of oxygen evolution electrocatalysts, *Nature* 593 (2021) 67-73.
- [11] F.M.F. de Groot, E. de Smit, M.M. van Schooneveld, L.R. Aramburo, B.M. Weckhuysen, In-situ Scanning Transmission X-Ray Microscopy of Catalytic Solids and Related Nanomaterials, *ChemPhysChem* 11 (2010) 951-962.
- [12] M. Guizar-Sicairos, P. Thibault, Ptychography: A solution to the phase problem, *Physics Today* 74 (2021) 42-48.
- [13] J. Rodenburg, A. Maiden, Ptychography, in: P.W. Hawkes, J.C.H. Spence (Eds.), *Springer Handbook of Microscopy*, Springer 2019.
- [14] F. Pfeiffer, X-ray ptychography, *Nature Photonics* 12 (2018) 9-17.
- [15] H.M.L. Faulkner, J.M. Rodenburg, Movable Aperture Lensless Transmission Microscopy: A Novel Phase Retrieval Algorithm, *Physical Review Letters* 93 (2004) 023903.
- [16] M. Farmand, R. Celestre, P. Denes, A.L.D. Kilcoyne, S. Marchesini, H. Padmore, T. Tyliszczak, T. Warwick, X. Shi, J. Lee, Y.-S. Yu, J. Cabana, J. Joseph, H. Krishnan, T. Perciano, F.R.N.C. Maia, D.A. Shapiro, Near-edge X-ray refraction fine structure microscopy, *Applied Physics Letters* 110 (2017) 063101.
- [17] D.A. Shapiro, S. Babin, R.S. Celestre, W. Chao, R.P. Conley, P. Denes, B. Enders, P. Enfedaque, S. James, J.M. Joseph, H. Krishnan, S. Marchesini, K. Muriki, K. Nowrouzi, S.R. Oh, H. Padmore, T. Warwick, L. Yang, V.V. Yashchuk, Y.-S. Yu, J. Zhao, An ultrahigh-resolution soft x-ray microscope for quantitative analysis of chemically heterogeneous nanomaterials, *Science Advances* 6 (2020) eabc4904.
- [18] C. Jacobsen, S. Wang, W. Yun, S. Frigo, Calculation of x-ray refraction from near-edge absorption data only, *Optical Science and Technology*, the SPIE 49th Annual Meeting, SPIE2004.
- [19] C. Jacobsen, *X-ray Microscopy*, Cambridge University Press, Cambridge, 2019.
- [20] E.M. Gullikson, X-ray Data Booklet Section 1.7 Atomic Scattering Factors, 2009.
- [21] B.L. Henke, E.M. Gullikson, J.C. Davis, X-Ray Interactions: Photoabsorption, Scattering, Transmission, and Reflection at $E = 50\text{-}30,000$ eV, $Z = 1\text{-}92$, *Atomic Data and Nuclear Data Tables* 54 (1993) 181-342.

- [22] B. Watts, Calculation of the Kramers-Kronig transform of X-ray spectra by a piecewise Laurent polynomial method, *Opt. Express* 22 (2014) 23628-23639.
- [23] S.-A. Zhou, A. Brahme, Development of phase-contrast X-ray imaging techniques and potential medical applications, *Physica Medica* 24 (2008) 129-148.
- [24] M. Dierolf, A. Menzel, P. Thibault, P. Schneider, C.M. Kewish, R. Wepf, O. Bunk, F. Pfeiffer, Ptychographic X-ray computed tomography at the nanoscale, *Nature* 467 (2010) 436-439.
- [25] A.M. Maiden, G.R. Morrison, B. Kaulich, A. Gianoncelli, J.M. Rodenburg, Soft X-ray spectromicroscopy using ptychography with randomly phased illumination, *Nature Communications* 4 (2013) 1669.
- [26] D.A. Shapiro, Y.-S. Yu, T. Tyliczszak, J. Cabana, R. Celestre, W. Chao, K. Kaznatcheev, A.L.D. Kilcoyne, F. Maia, S. Marchesini, Y.S. Meng, T. Warwick, L.L. Yang, H.A. Padmore, Chemical composition mapping with nanometre resolution by soft X-ray microscopy, *Nature Photonics* 8 (2014) 765-769.
- [27] M. Farmand, R. Celestre, P. Denes, A.L.D. Kilcoyne, S. Marchesini, H. Padmore, T. Tyliczszak, T. Warwick, X. Shi, J. Lee, Y.-S. Yu, J. Cabana, J. Joseph, H. Krishnan, T. Perciano, F.R.N.C. Maia, D.A. Shapiro, Near-edge X-ray refraction fine structure microscopy, *Applied Physics Letters* 110 (2017).
- [28] K.V. Kaznatcheev, C. Karunakaran, U.D. Lanke, S.G. Urquhart, M. Obst, A.P. Hitchcock, Soft X-ray spectromicroscopy beamline at the CLS: Commissioning results, *Nuclear Instruments and Methods in Physics Research Section A: Accelerators, Spectrometers, Detectors and Associated Equipment* 582 (2007) 96-99.
- [29] T. Sun, G. Sun, F. Yu, Y. Mao, R. Tai, X. Zhang, G. Shao, Z. Wang, J. Wang, J. Zhou, Soft X-ray Ptychography Chemical Imaging of Degradation in a Composite Surface-Reconstructed Li-Rich Cathode, *ACS Nano* 15 (2021) 1475-1485.
- [30] J.M. Rodenburg, H.M.L. Faulkner, A phase retrieval algorithm for shifting illumination, *Applied Physics Letters* 85 (2004) 4795-4797.
- [31] F. Zhang, I. Peterson, J. Vila-Comamala, A. Diaz, F. Berenguer, R. Bean, B. Chen, A. Menzel, I.K. Robinson, J.M. Rodenburg, Translation position determination in ptychographic coherent diffraction imaging, *Opt. Express* 21 (2013) 13592-13606.
- [32] J.R. Fienup, Reconstruction of an object from the modulus of its Fourier transform, *Opt. Lett.* 3 (1978) 27-29.
- [33] P. Thibault, A. Menzel, Reconstructing state mixtures from diffraction measurements, *Nature* 494 (2013) 68-71.
- [34] A.P. Hitchcock, aXis2000, Hamilton, ON, 2023.
- [35] `scipy.fftpack.hilbert`, docs.scipy.org, 2023.
- [36] D. Covelli, D. Hernández-Cruz, B.M. Haines, V. Munoz, O. Omotoso, R. Mikula, S. Urquhart, NEXAFS microscopy studies of the association of hydrocarbon thin films with fine clay particles, *Journal of Electron Spectroscopy and Related Phenomena* 173 (2009) 1-6.

(a)



(b)

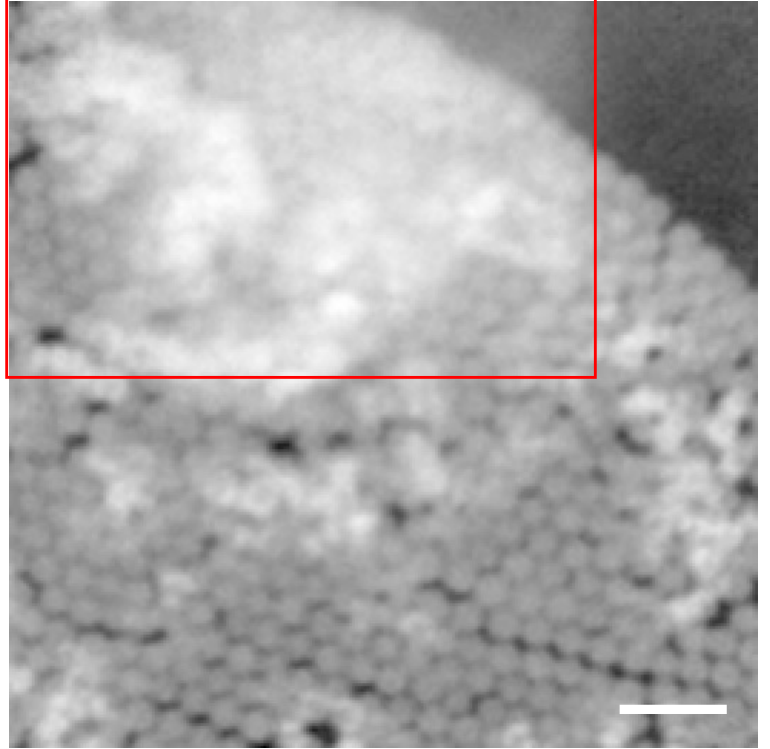


Figure 1

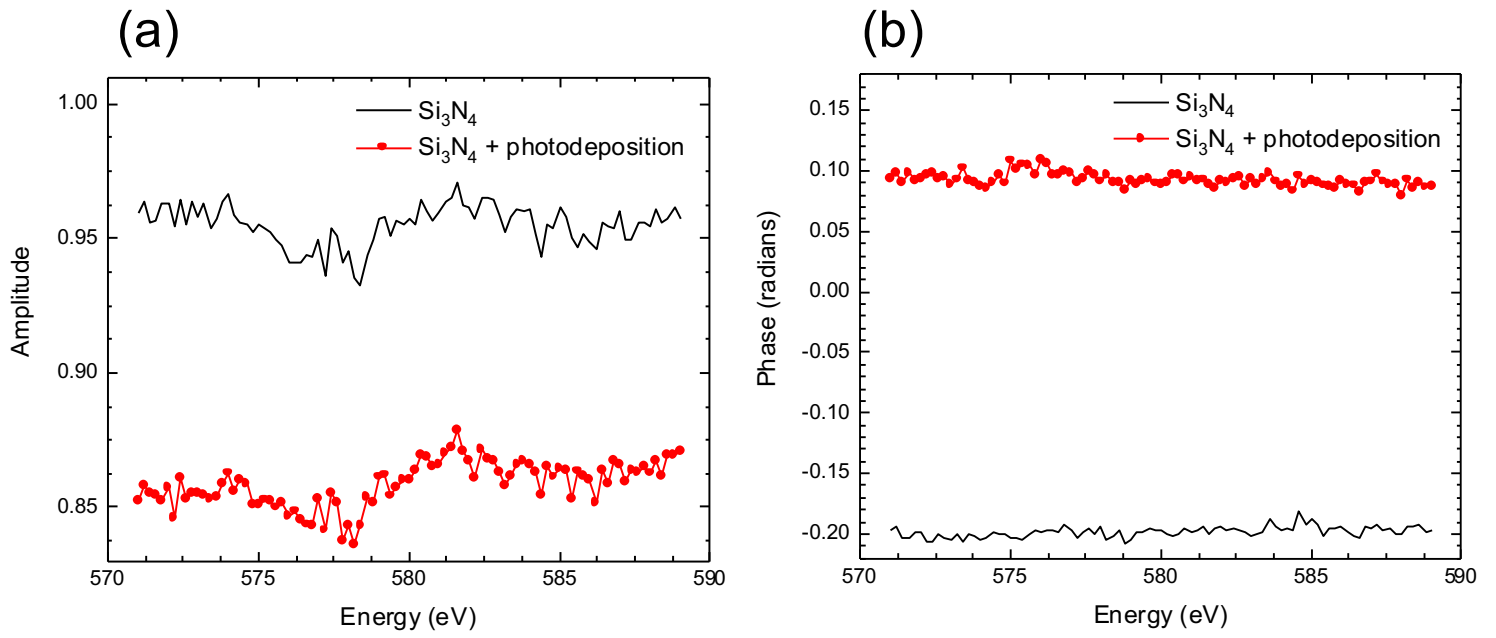


Figure 2

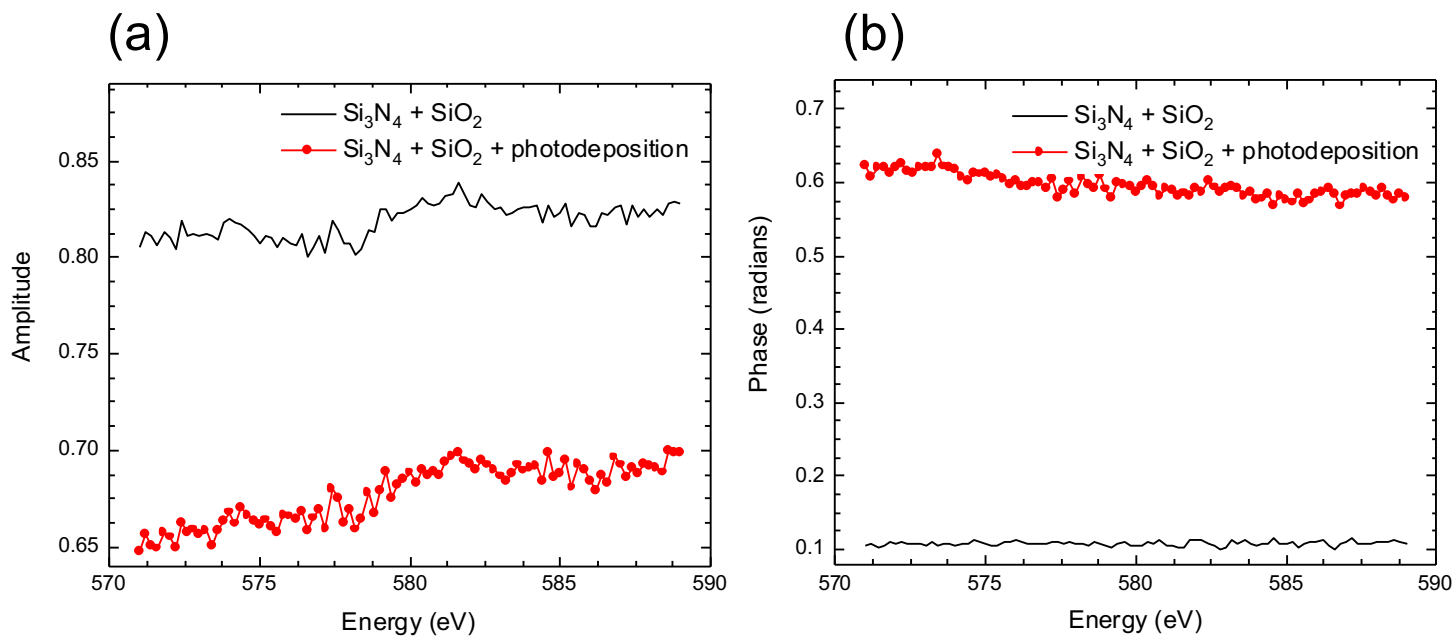


Figure 3

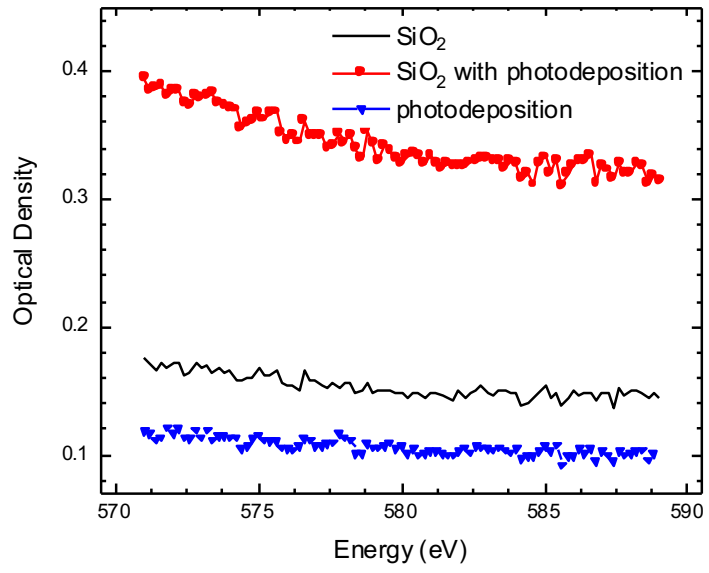


Figure 4

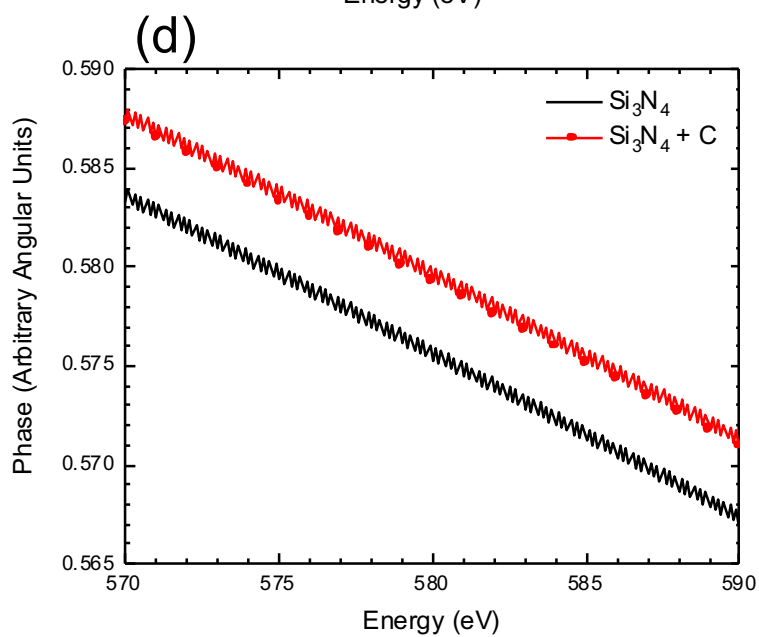
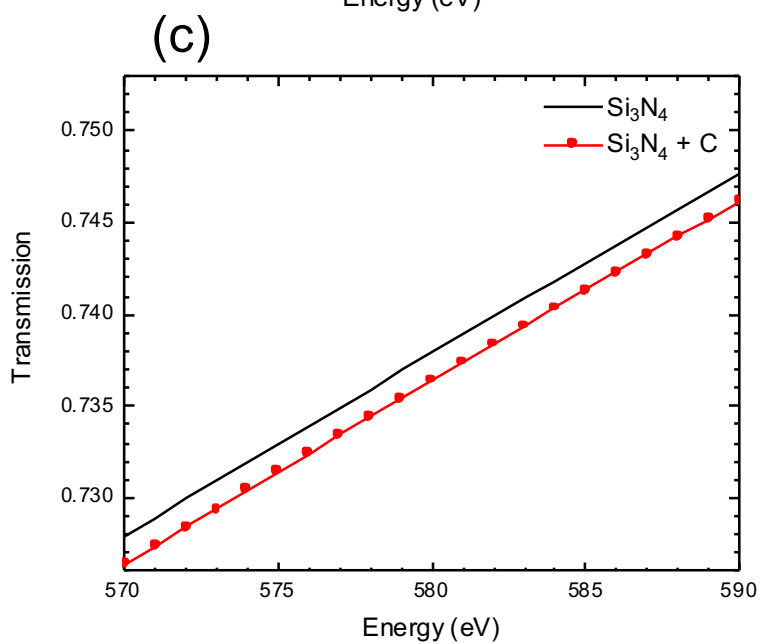
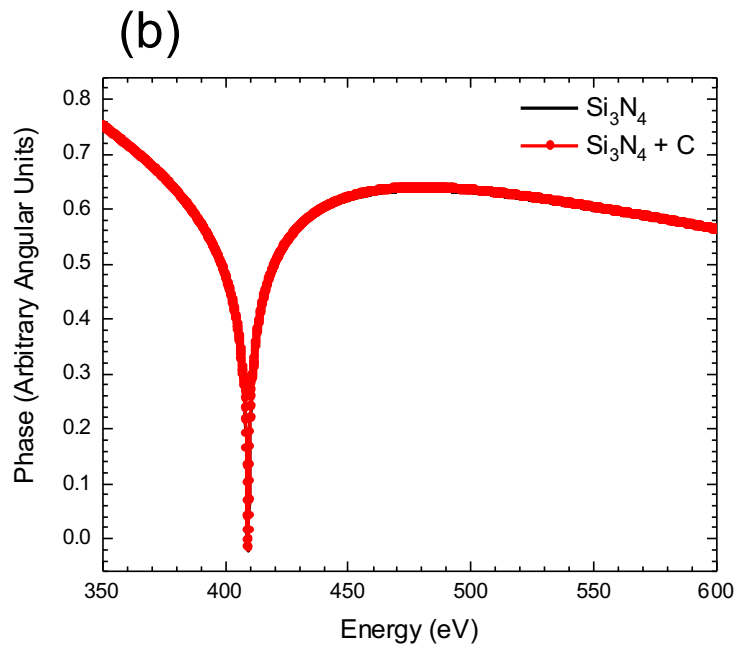
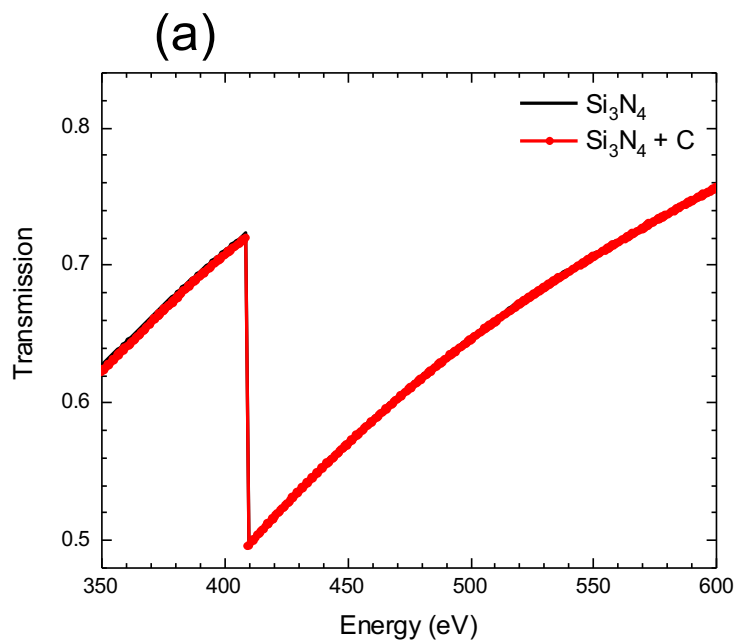


Figure 5

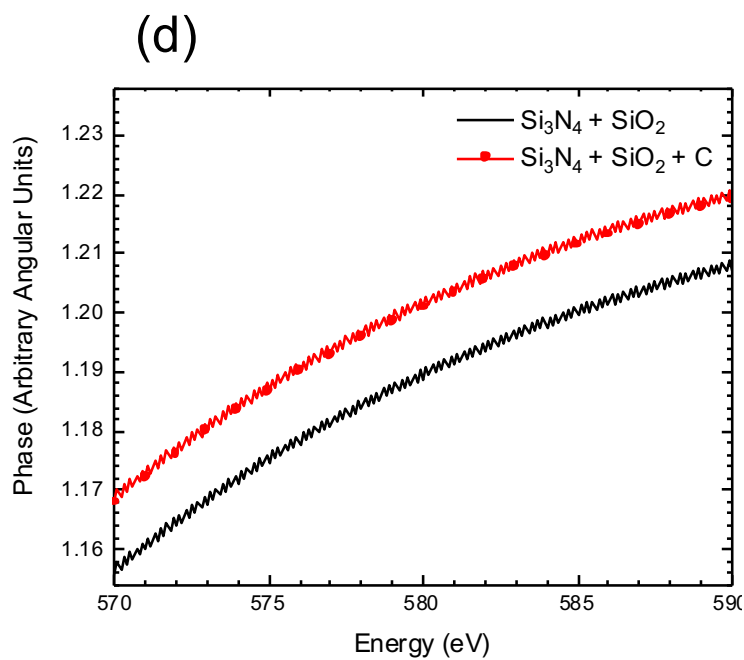
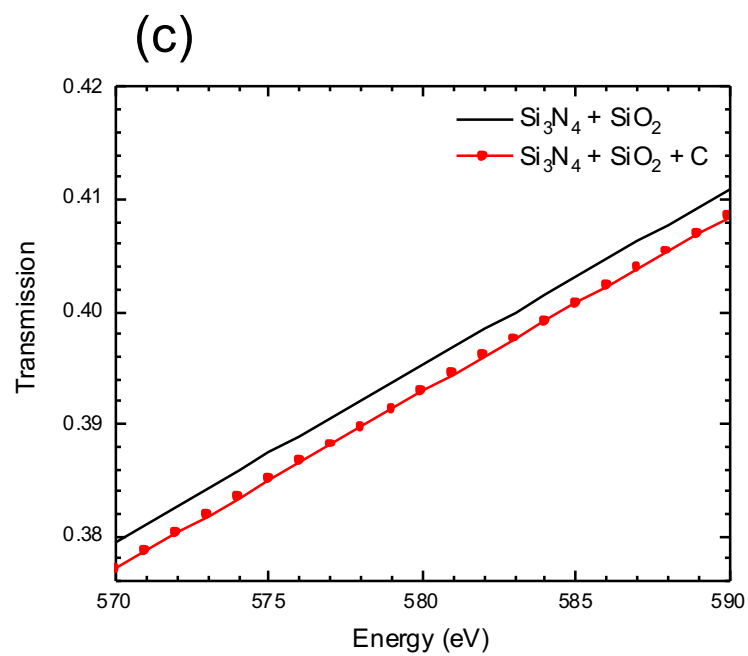
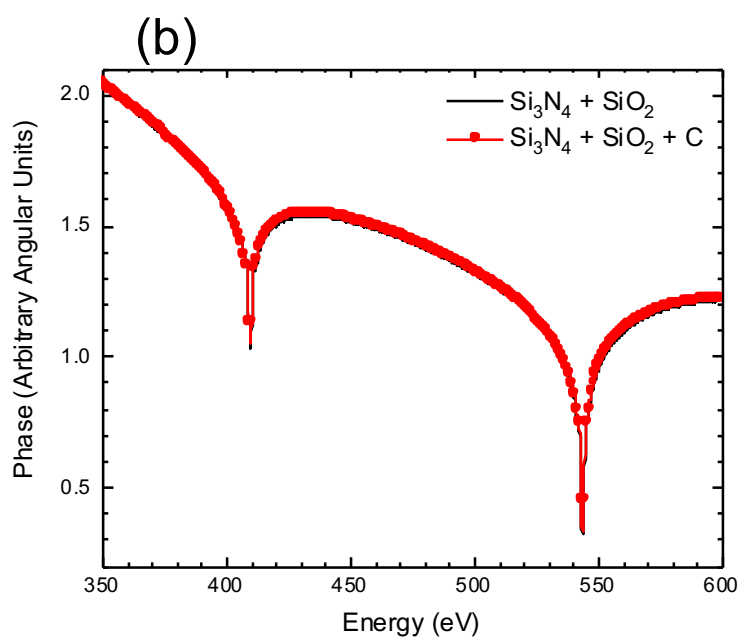
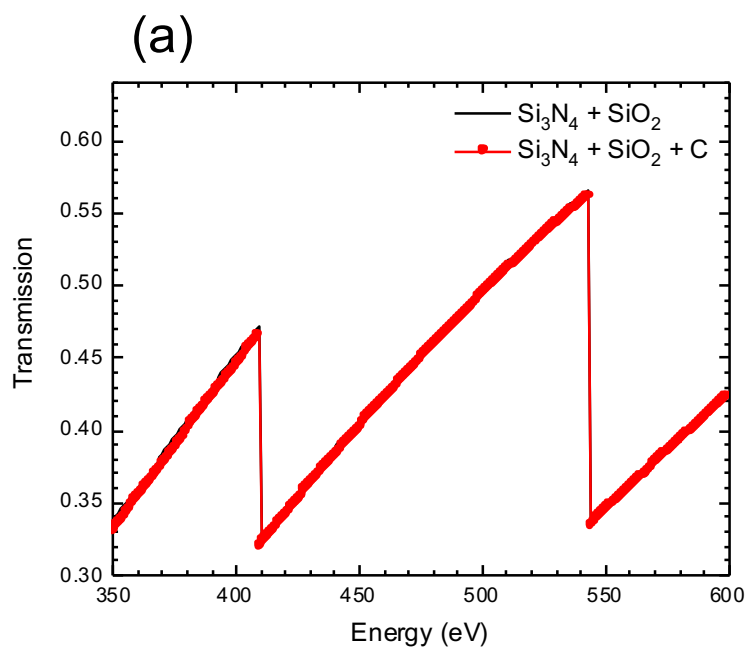


Figure 6

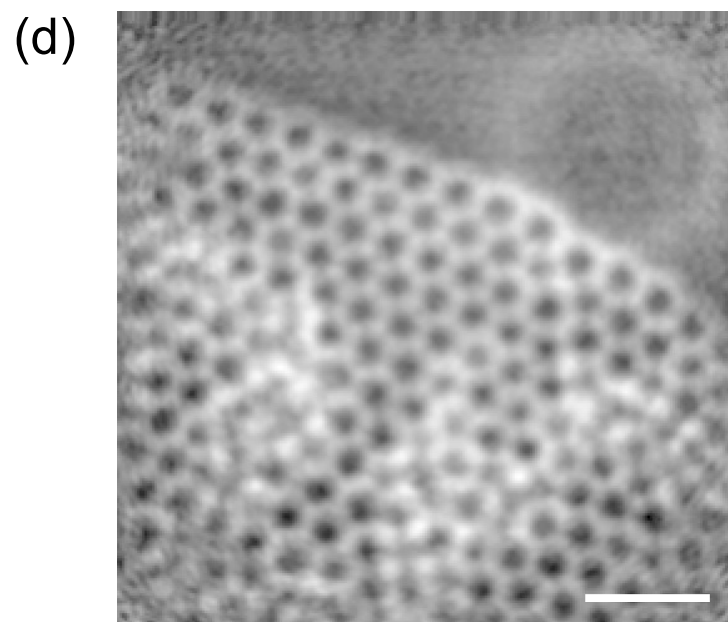
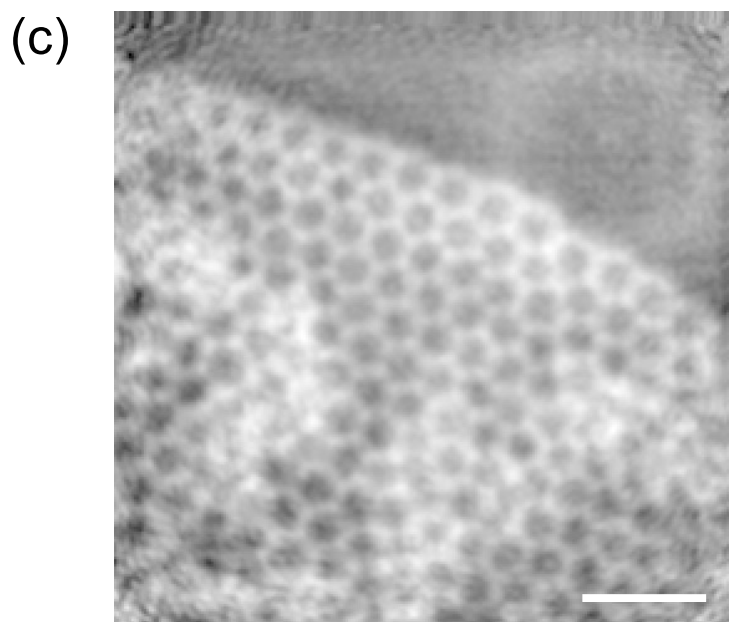
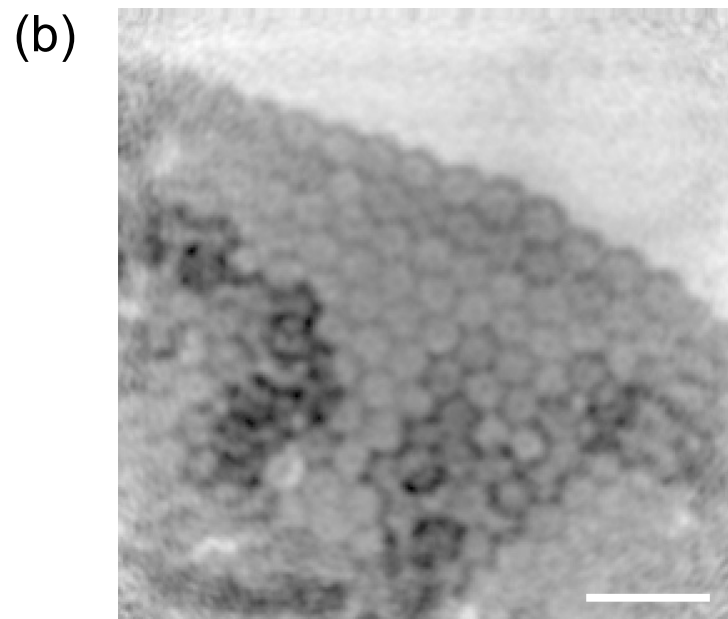
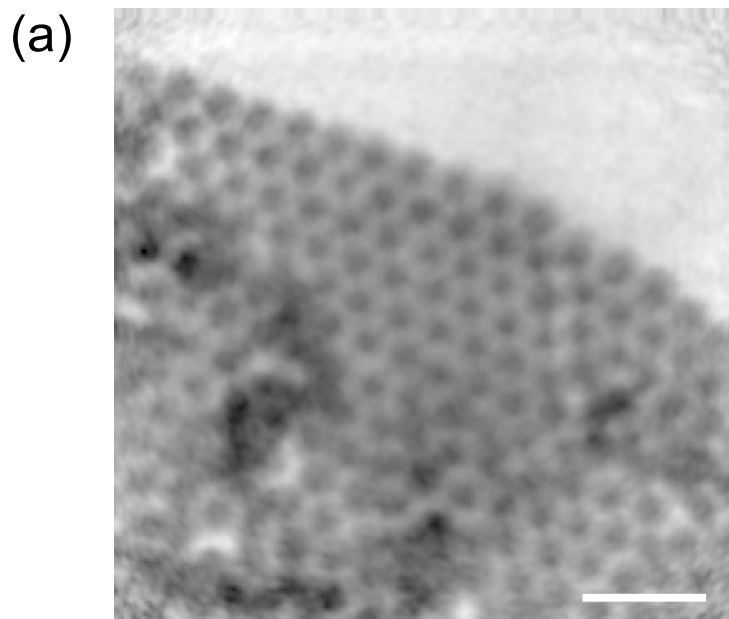


Figure 7

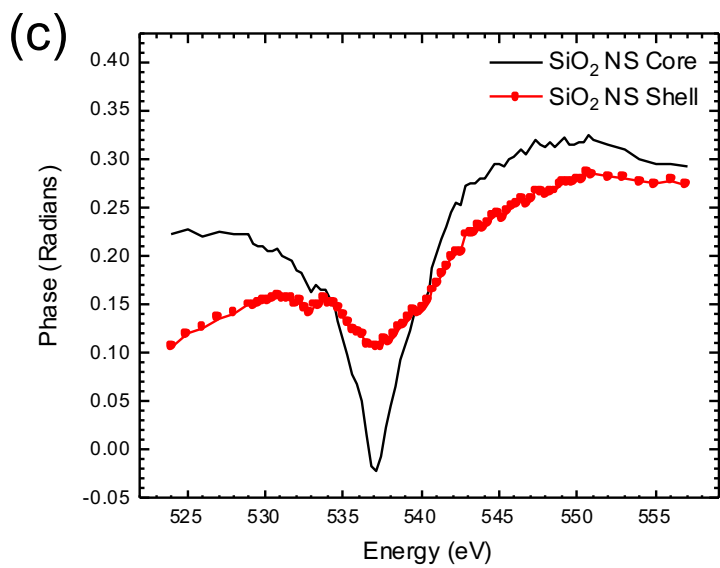
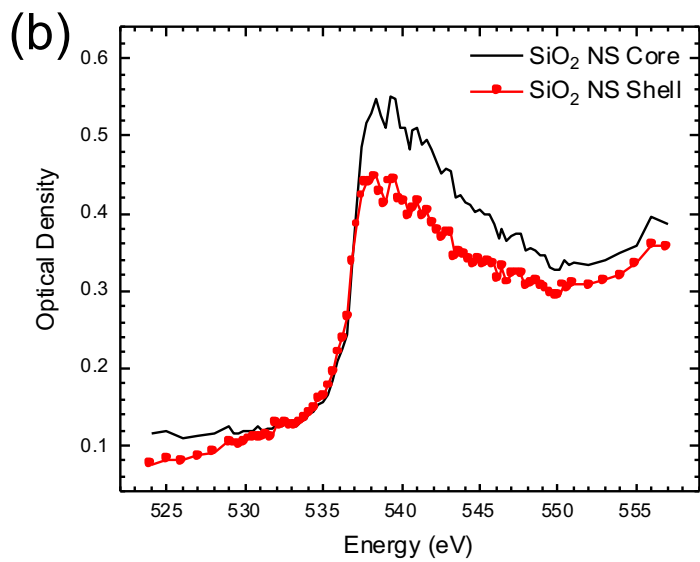
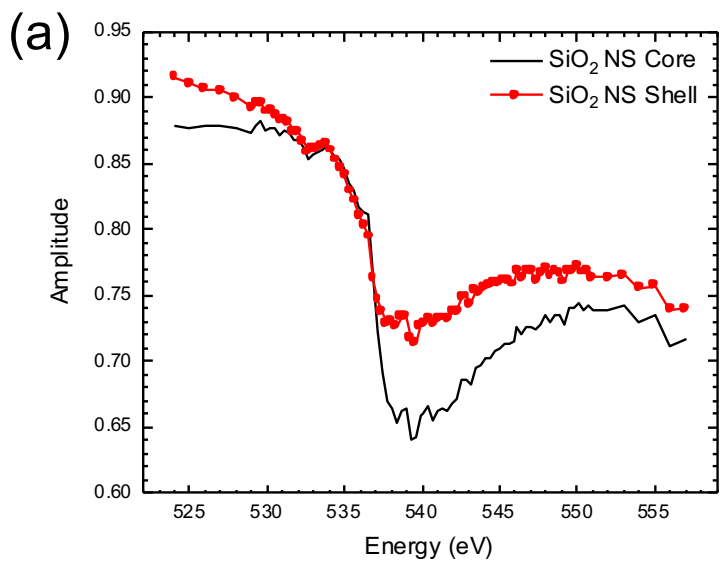
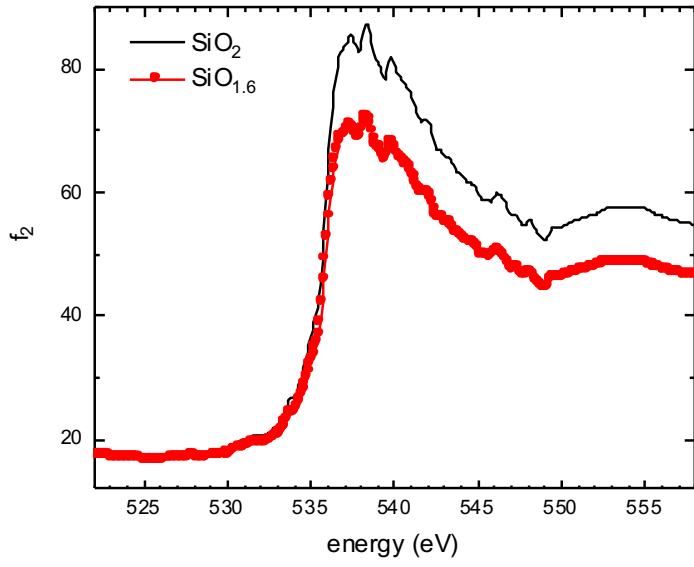


Figure 8

(a)



(b)

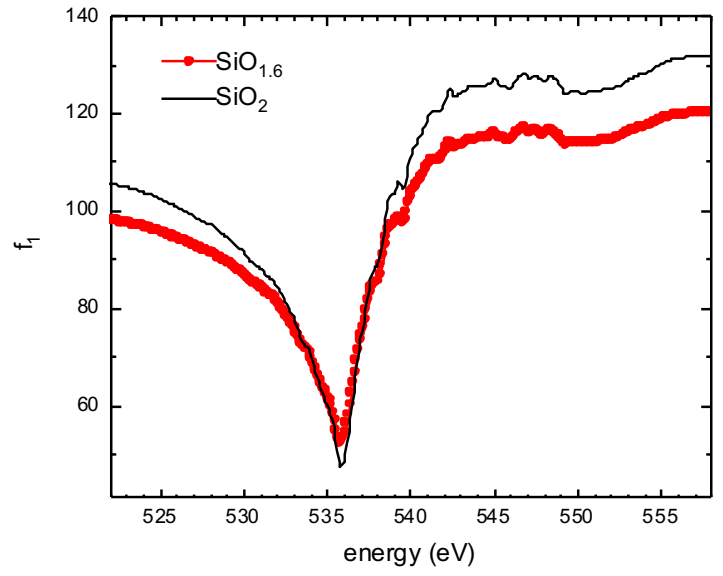


Figure 9